Nonlinear Dyn
https://doi.org/10.1007/s11071-019-04959-x

ORIGINAL PAPER

Modeling and identification of electro-elastic nonlinearities in ultrasonic power transfer systems

Vamsi C. Meesala · Muhammad R. Hajj · Shima Shahab

Received: 11 December 2018 / Accepted: 15 April 2019
© Springer Nature B.V. 2019

Abstract We establish a nonlinear non-conservative mathematical framework for the acoustic-electro-elastic dynamics of the response of a piezoelectric disk to high-level acoustic excitation in the context of ultrasound acoustic energy transfer. Nonlinear parameter identification is performed to estimate the parameters representing nonlinear piezoelectric coefficients. The identification is based on exploiting the vibrational response of the disk operating in the thickness mode under dynamic actuation. The nonlinearly coupled electro-elastic governing equations, for the piezoelectric receiver subjected to acoustic excitation, are derived using the generalized Hamilton's principle. The method of multiple scales is used to obtain an approximate solution that forms the basis for parameter identification. The identified coefficients are then experimentally validated. The effects of varying these coefficients on the nonlinear response, optimal resistive electrical loading, and power generation characteristics of the receiver are investigated.

Keywords Ultrasound acoustic energy transfer · Contactless power transfer · Piezoelectric materials · Method of multiple scales · Material nonlinearity · Optimal resistive electrical loading

1 Introduction

Contactless power transfer (CPT) has become a topic of interest over the past decade because it eliminates dissipation losses in conducting wires and its advantage as a maintenance-free operation in aerospace, biomedicine, and microsensor applications [1,2]. Some well-studied CPT techniques include inductive [3], capacitive coupling [4], and far-field electromagnetic energy transfer [5], which use electromagnetic waves for wireless energy transfer. These methods can achieve high efficiency at close transmitter-to-receiver distances but often perform poorly as the distance between transmitter and receiver increases [6]. More recently, ultrasound acoustic energy transfer (UAET) was proposed as a transformative CPT approach for application in biomedical devices [7–13] and sensing networks in enclosed containers or space stations [14–16]. In UAET, energy is transferred through the reception of acoustic waves by a piezoelectric receiver that converts the mechanical energy induced by incident acoustic waves to electrical voltage. Thorough litera-

V. C. Meesala · S. Shahab
Department of Biomedical Engineering and Mechanics, Virginia Tech, 495 Old Turner Street, Norris Hall, Blacksburg, VA 24060, USA

S. Shahab (✉)
Department of Mechanical Engineering, 445 Goodwin Hall, 635 Prices Fork Road - MC 0238, Blacksburg, VA 2406, USA
e-mail: sshahab@vt.edu

M. R. Hajj
Davidson laboratory, Department of Civil, Environmental and Ocean Engineering, Stevens Institute of Technology, 711 Hudson St, Hoboken, NJ 07030, USA

Published online: 25 April 2019

ture reviews on UAET and its advantages over inductive, microwave, capacitive, and optical energy transfer methods have been presented by Roes et al. [6], Zaid et al. [17], and Awal et al. [18].

To date, research of UAET systems has been limited to modeling and proof-of-concept experiments, mostly in linear regime, i.e., under small levels of acoustic pressure that result in small-amplitude longitudinal vibrations and linearized piezoelectricity [14,15,19–25]. Shahab and Erturk [19] considered an incident acoustic wave, originating from a spherical source of known strength, and developed a multi-physics model to analyze the electrical power output extracted by a piezoelectric receiver in fixed–free boundary conditions and validated it with finite element simulations. Shahab et al. [20] later experimentally validated the theoretical framework for free–free boundary conditions. Gorostiaga et al. [21] considered a piezoelectric receiver that is acoustically excited with a plane wave and performed a theoretical study to determine the optimum electrical load by zero reflections and power maximization approaches. They showed that both approaches predict same optimum load for a lossless transducer but differ as the losses increase. They also validated their results with experiments [22]. All of the previously discussed studies assume a linear piezoelectric constitutive relation [19]. Response predictions using this assumption fail under high acoustic excitation levels due to the acoustic medium and the receiver's geometric and electro-elastic nonlinearities. When the amplitude of the acoustic wave becomes sufficiently large, the waves become distorted due to the generation of higher harmonics as they propagate in the medium [26,27]. When the induced strains are high in the piezoelectric receiver, material nonlinearities and nonlinear coupling with the electric field become important [28–34]. Under such conditions, there is a need to account for both acoustic nonlinearities of the medium and material electro-elastic nonlinearities to accurately determine the receiver's response and output voltage.

The objective of this effort is to investigate the effects of material electro-elastic nonlinear parameters of the piezoelectric receiver on the electrical power output in UAET systems. To this end, we develop an acoustic-electro-elastic model of the receiver using a nonlinear constitutive relation. We neglect the effects of absorption, diffraction, and nonlinear distortion in the medium, as they are not the main focus of this effort. The governing and electrical circuit equations are determined using the generalized Hamilton's principle followed by a Galerkin's discretization. The wave–structure interaction is approximated as the net effect of an incident acoustic wave and the acoustic radiation impedance of a baffled circular piston [35,48]. Approximate solutions of the discretized governing and circuit equations are obtained using the method of multiple scales [36,37]. We use these solutions to implement a parameter identification scheme that determines the nonlinear material coefficients. We validate the identified coefficients with experiments and preform a detailed analysis to determine the effects of nonlinearity on the vibration response and electrical power output characteristics of the piezoelectric receiver.

2 Mathematical modeling

To analyze the electromechanical response characteristics of the piezoelectric receiver, we consider a disk of thickness l, radius r_0, and mass per unit length m, that is connected to a load resistance R, operating in the thickness mode as shown in Fig. 1. The acoustic medium has a density ρ_0 and speed of sound c_0 . The receiver, with free–free boundary conditions, is excited with a spherical acoustic source of radius r_{source} and source strength Q. The governing and electrical circuit equations of the coupled electromechanical system are derived using the generalized Hamilton's principle [30,38–41], which is written as

$$\int_{t_1}^{t_2} \delta(T - \Delta + W_{\text{nc}})\,\mathrm{d}t = 0, \tag{1}$$

where T, Δ, and W_{nc} are, respectively, the kinetic energy, electromechanical enthalpy, and work done by non-conservative or external forces. Here, δ is the variation operator.

Denoting the displacement of an integral element of the receiver at s by $u(s,t)$, the kinetic energy of the receiver is written as

$$T = \frac{1}{2}\int_0^l m\dot{u}^2\,\mathrm{d}s, \tag{2}$$

where the overdot is used to represent the derivative with respect to time. The variation of kinetic energy is then written as

$$\delta T = \int_0^l m\dot{u}\delta\dot{u}\,\mathrm{d}s. \tag{3}$$

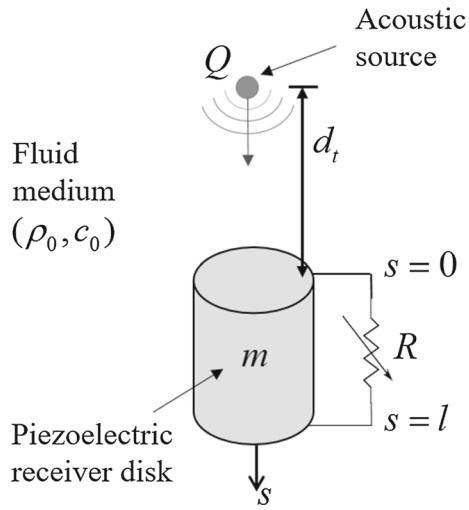

Fig. 1 Schematic of the piezoelectric receiver

Analysis of the vibration characteristics of piezoelectric disk actuators has been extensively investigated in the literature [19,20,42–47]. Most theoretical models assume that the displacement is in the thickness direction as one-dimensional. However, experiments show that the one-dimensional assumption is accurate only when the diameter-to-thickness ratio $(2r_0/l)$ is larger than 20 or smaller than 0.5 [42–44]. By performing experiments on $PbTiO_3$ disks, Ikegami et al. [43] classified the modal vibrational response into five groups. They are thickness extensional, shear, edge, radial, and high-frequency radial modes. Because a closed-form solution for the three-dimensional model cannot be easily obtained for a thin disk, the mixed modal behavior could only be determined from either experiments or finite element method simulations [44–47].

In order to assess the effects of material nonlinearity on the electromechanical response of the receiver, we assume that the piezoelectric receiver vibrates in the thickness direction only and is subjected to a "piston-like" motion, wherein the radial, edge, thickness shear, and thickness extensional modes are all neglected [47]. The one-dimensional axial strain at any position, s, is then defined by

$$\varepsilon_{33}(s,t) = \frac{\partial}{\partial s} u(s,t). \tag{4}$$

Considering that the thickness of receiver is in the 3-direction and neglecting the effect of Poisson's ratio enable us to neglect all strains expect ε_{33}. Then, the electromechanical enthalpy per unit volume is given by [30]

$$\begin{aligned}\Delta = &\int_0^l \frac{1}{2} Y_{33} A \varepsilon_{33}^2 \,\mathrm{d}s - \int_0^l e_{33} A \varepsilon_{33} E_3 \,\mathrm{d}s \\ &- \int_0^l \frac{1}{2} \alpha_3 A E_3 \varepsilon_{33}^2 \,\mathrm{d}s - \int_0^l \frac{1}{2} \epsilon_{33}^S A E_3^2 \,\mathrm{d}s \\ &+ \int_0^l \frac{1}{6} \alpha_1 A \varepsilon_{33}^3 \,\mathrm{d}s - \int_0^l \frac{1}{6} \alpha_2 A \varepsilon_{33}^3 E_3 \,\mathrm{d}s \\ &+ \int_0^l \frac{1}{8} \alpha_4 A \varepsilon_{33}^4 \,\mathrm{d}s,\end{aligned} \tag{5}$$

where Y_{33}, e_{33}, and ϵ_{33}^S are, respectively, the elastic modulus (for thickness mode), piezoelectric coupling coefficient, and dielectric (or piezoelectric permittivity) constant. The coefficients α_1, α_2, α_3, and α_4 represent the nonlinear material properties. Here, E_3 is the induced electric field due to the strain induced in the receiver in the 3-direction and can be related to generated electric potential by

$$\begin{aligned}E_3(s,t) &= -\frac{V(t)}{l}\left[H(s) - H(s-l)\right] \\ &\equiv -\frac{V_H(s,t)}{l},\end{aligned} \tag{6}$$

where $H(s)$ is the Heaviside step function and $[H(s) - H(s-l)]$ is used to denote that the electric field is constant through the thickness of the receiver. Substituting Eqs. (4) and (6) into Eq. (5), we obtain the variation of electromechanical enthalpy as

$$\begin{aligned}\delta\Delta = &\int_0^l Y_{33} A u' \delta u' \,\mathrm{d}s + \int_0^l e_{33} A \delta u' \frac{V_H}{l} \,\mathrm{d}s \\ &+ \int_0^l e_{33} A u' \frac{\delta V_H}{l} \,\mathrm{d}s \\ &+ \int_0^l \alpha_3 A \frac{V_H}{l} u' \delta u' \,\mathrm{d}s + \int_0^l \frac{1}{2} \alpha_3 A \frac{\delta V_H}{l} u'^2 \,\mathrm{d}s \\ &- \int_0^l \epsilon_{33}^S A \frac{V_H \delta V_H}{l^2} \,\mathrm{d}s \\ &+ \int_0^l \frac{1}{2} \alpha_1 A u'^2 \delta u' \,\mathrm{d}s + \int_0^l \frac{1}{2} \alpha_2 A u'^2 \delta u' \frac{V_H}{l} \,\mathrm{d}s \\ &+ \int_0^l \frac{1}{6} \alpha_2 A u'^3 \frac{\delta V_H}{l} \,\mathrm{d}s \\ &+ \int_0^l \frac{1}{2} \alpha_4 A u'^3 \delta u' \,\mathrm{d}s.\end{aligned} \tag{7}$$

Assuming that the acoustic excitation is generated by a spherical acoustic source ($k_0 r_{source} << 1$), the pressure on the top surface of the disk is given by

$$p_{\mathrm{t}}(t) \approx j\rho_0 c_0 k_0 \frac{Q}{4\pi}\frac{1}{d_{\mathrm{t}}} e^{j(\Omega t - k_0 d_{\mathrm{t}})} = j\rho_0 \Omega \frac{Q}{4\pi}\frac{1}{d_{\mathrm{t}}} e^{j(\Omega t - k_0 d_{\mathrm{t}})}, \tag{8a}$$

and the pressure on the bottom surface is given by

$$p_{\mathrm{b}}(t) \approx j\rho_0 \Omega \frac{Q}{4\pi}\frac{1}{d_{\mathrm{t}}+l} e^{j(\Omega t - k_0 d_{\mathrm{t}} - k_0 l)} = \chi p_{\mathrm{t}} e^{-j\Omega\tau}, \tag{8b}$$

$$\chi = \frac{d_{\mathrm{t}}}{d_{\mathrm{t}}+l}, \text{ and } \quad \tau = \frac{l}{c_0}, \tag{8c}$$

where d_{t} is the distance from source to the top surface of the disk, and $k_0 = \Omega/c_0$.

The acoustic radiation impedance, Z_{r}, that represents the reaction forces induced in the medium as a result of the motion of receiver's surfaces [48], is defined as

$$Z_{\mathrm{r}} = -\frac{F_{\mathrm{r}}}{\dot{u}} = \frac{1}{\dot{u}} \iint_S p(\mathbf{r})\, \mathrm{d}S = R_{\mathrm{r}} + jX_{\mathrm{r}}, \tag{9a}$$

where R_{r} and X_{r} represent the radiation resistance and reactance terms, respectively. They are given by the following relations for a baffled circular piston [48]:

$$R_{\mathrm{r}} = \rho_0 c_0 A\left[1 - \frac{J_1(2k_0 r_0)}{k_0 r_0}\right], \text{ and } \quad X_{\mathrm{r}} = \rho_0 c_0 A \frac{S_1(2k_0 r_0)}{k_0 r_0}, \tag{9b}$$

where J_1 and S_1 are, respectively, the first-order Bessel and Struve functions. The acoustic radiation resistance and reactance for an unbaffled circular piston are calculated vs. $k_0 r_0$ and presented in Fig. 2. The radiation resistance (R_{r}) represents the transfer of power from the vibrating receiver to the fluid medium, whereas the radiation reactance (X_{r}) increases the kinetic energy of the system, which subsequently shifts the natural frequency and alters the mode shapes. Therefore, we define the radiation mass as $m_{\mathrm{r}} = X_{\mathrm{r}}/\omega$ [48].

The variational work by non-conservative forces—structural damping, acoustic–structure interaction (pressure excitation and radiation impedance) [20]—is written as

$$\begin{aligned}\delta W = {} & f_{\mathrm{t}}(t)\delta u(0,t) - f_{\mathrm{b}}(t)\delta u(l,t) \\ & - \int_0^l c_{\mathrm{s}}\dot{u}(s,t)\delta u(s,t)\,\mathrm{d}s - R_{\mathrm{r}}\dot{u}(0,t)\delta u(0,t) \\ & - jm_{\mathrm{r}}\omega\dot{u}(0,t)\delta u(0,t) - R_{\mathrm{r}}\dot{u}(l,t)\delta u(l,t) \\ & - jm_{\mathrm{r}}\omega\dot{u}(l,t)\delta u(l,t) - \Psi\delta V,\end{aligned} \tag{10}$$

where $f_{\mathrm{t}}\left(= \int_0^{r_0} 2\pi r p_{\mathrm{t}}\, dr\right)$ and f_{b} are, respectively, the forces on top and bottom surfaces, and c_{s} and Ψ are, respectively, the structural damping coefficient and the net generated electric charge. As the excitation and response of the system are harmonic functions and that $j\omega\dot{u} = \ddot{u}$, Eq. (10) is rewritten as

$$\begin{aligned}\delta W = {} & f_{\mathrm{t}}(t)\delta u(0,t) - f_{\mathrm{b}}(t)\delta u(l,t) \\ & - \int_0^l c_{\mathrm{s}}\dot{u}(s,t)\delta u(s,t)\,\mathrm{d}s \\ & - R_{\mathrm{r}}\dot{u}(0,t)\delta u(0,t) - m_{\mathrm{r}}\ddot{u}(0,t)\delta u(0,t) \\ & - R_{\mathrm{r}}\dot{u}(l,t)\delta u(l,t) \\ & - m_{\mathrm{r}}\ddot{u}(l,t)\delta u(l,t) - \Psi\delta V.\end{aligned} \tag{11}$$

Substituting Eqs. (3), (7), and (11) into Eq. (1) and performing integration by parts, we obtain the governing equation:

$$\begin{aligned}& -m\ddot{u} + Y_{33}Au'' + e_{33}A\frac{V'}{l} \\ & + \alpha_3 A\left(\frac{V}{l}u'' + \frac{V'}{l}u'\right) + \alpha_1 Au'u'' \\ & + \frac{1}{2}\alpha_2 A\left(u'^2\frac{V'}{l} + 2u'u''\frac{V}{l}\right) \\ & + \frac{3}{2}\alpha_4 Au'^2u'' - c_{\mathrm{s}}\dot{u} + f_{\mathrm{t}}\delta[s] - f_{\mathrm{b}}\delta[s-l] \\ & - R_{\mathrm{r}}\dot{u}\delta[s] - R_{\mathrm{r}}\dot{u}\delta[s-l] = 0,\end{aligned} \tag{12}$$

the corresponding electrical circuit equation

$$\int_0^l \left[-\frac{1}{2}\alpha_3 A\frac{1}{l}u'^2 - e_{33}Au'\frac{1}{l} + \epsilon_{33}^S A\frac{V}{l^2} - \frac{1}{6}\alpha_2 Au'^3\frac{1}{l}\right]\mathrm{d}s - \Psi = 0, \tag{13}$$

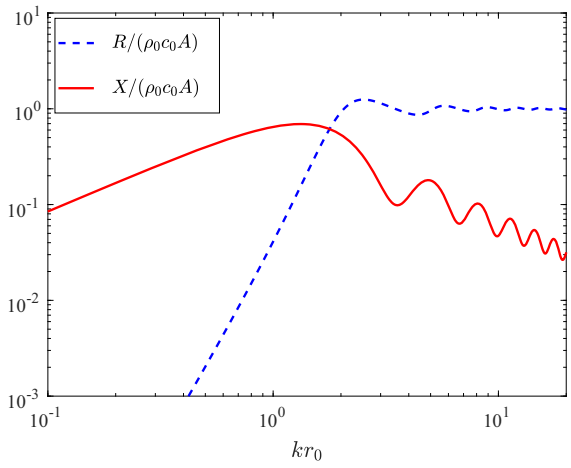

Fig. 2 Normalized radiation resistance $R_{\mathrm{r}}/(\rho_0 c_0 A)$, and reactance $X_{\mathrm{r}}/(\rho_0 c_0 A)$ for $0 \le k_0 r_0 \le 20$ of a baffled piston

the natural boundary condition on the top surface, $s = 0$

$$-m_{\mathrm{r}}\ddot{u} + Y_{33}Au' + e_{33}A\frac{V}{l} + \alpha_3 A\frac{V}{l}u' + \frac{1}{2}\alpha_1 Au'^2 + \frac{1}{2}\alpha_2 Au'^2\frac{V}{l} + \frac{1}{2}\alpha_4 Au'^3\Big|_{s=0} = 0, \tag{14}$$

and the natural boundary condition on the bottom surface, $s = l$

$$-m_{\mathrm{r}}\ddot{u} - Y_{33}Au' - e_{33}A\frac{V}{l} - \alpha_3 A\frac{V}{l}u' - \frac{1}{2}\alpha_1 Au'^2 - \frac{1}{2}\alpha_2 Au'^2\frac{V}{l} - \frac{1}{2}\alpha_4 Au'^3\Big|_{s=l} = 0. \tag{15}$$

2.1 Governing equation of temporal modes

The linear, undamped, short-circuit and unforced governing equation as well as the boundary conditions are written as

$$-m\ddot{u} + Y_{33}Au'' = 0, \tag{16a}$$

$$-m_{\mathrm{r}}\ddot{u} + Y_{33}Au'\big|_{s=0} = 0, \text{ and } -m_{\mathrm{r}}\ddot{u} - Y_{33}Au'\big|_{s=l} = 0. \tag{16b}$$

The general solution for Eq. (16a) is

$$u(s,t) = \frac{1}{2}a_+ e^{j(ks-\omega t)} + \frac{1}{2}a_- e^{j(-ks-\omega t)} + c.c, \tag{17}$$

where $k = \omega\sqrt{\frac{m}{Y_{33}A}}$ and a_+, a_-, and ω represent the complex amplitudes of forward and backward traveling waves and the natural frequency of the receiver, respectively. Substituting the general solution presented in Eq. (17) in (16b), we obtain

$$\frac{m_{\mathrm{r}}}{m}k(a_+ + a_-) + (a_+ - a_-) = 0, \text{ and} \tag{18a}$$

$$\frac{m_{\mathrm{r}}}{m}k(a_+ e^{2jkl} + a_-) + j(a_+ e^{2jkl} - a_-) = 0. \tag{18b}$$

Simplifying Eqs. (18a) and (18b), we obtain

$$\frac{a_{i-}}{a_{i+}} = \frac{1 - jk_i\frac{m_{\mathrm{r}}}{m}}{1 + jk_i s\frac{m_{\mathrm{r}}}{m}}, \text{ and } k_i = \frac{i\pi}{l}, \text{ and } i = 1, 2, 3 \ldots \infty. \tag{19}$$

Equation (19) shows that there are infinite thickness modes for the receiver and, as such, the solution is written as

$$u(s,t) = \sum_{i=1}^{\infty}\frac{2a_{i+}}{1 + k_i^2\left(\frac{m_{\mathrm{r}}}{m}\right)^2}\left[\cos(k_i s) - \frac{m_{\mathrm{r}}}{m}k_i \sin(k_i s)\right]e^{-j\omega_i t} \tag{20a}$$

which can be rewritten as

$$u(s,t) = \sum_{i=1}^{\infty}\hat{a}_i\left[\cos(k_i s) - \frac{m_{\mathrm{r}}}{m}k_i \sin(k_i s)\right]q(t) \equiv \sum_{i=1}^{n}\phi_i(s)q_i(t), \tag{20b}$$

where $\phi_n(s)$ is the nth mode shape and $q_n(t)$ is the corresponding temporal amplitude. For two distinct modes p and q, Eq. (16a) in conjunction with the linear boundary conditions presented in Eq. (16b) yields [49]

$$m_{\mathrm{r}}\phi_q\phi_q|_{s=l} + m_{\mathrm{r}}\phi_q\phi_q|_{s=0} + \int_0^l m\phi_p\phi_q\,\mathrm{d}s = \delta_{pq} \tag{21a}$$

and, subsequently,

$$\int_0^l Y_{33}A\phi_p'\phi_q'\,\mathrm{d}s = \delta_{pq}\omega_p^2. \tag{21b}$$

To obtain the governing equation of the temporal amplitude, we use the solution of the linear system and follow the Galerkin's weighted residual method. So, we substitute Eq. (20b) in the nonlinear distributed parameter governing equation (12) followed by multiplying equation with $\phi_j(s)$ and integrating over the thickness of the disk, which yields

$$\int_0^l \phi_k\left(-m\sum_{i=1}^{n}\phi_i\ddot{q}_i + Y_{33}A\sum_{i=1}^{n}\phi_i''q_i + e_{33}A\frac{V_H'}{l} + \alpha_1 A\sum_{i=1}^{n}\phi_i''q_i\sum_{j=1}^{n}\phi_j'q_j + \alpha_3 A\left[\frac{V_H}{l}\sum_{i=1}^{n}\phi_i''q_i + \frac{V_H'}{l}\sum_{i=1}^{n}\phi_i'q_i\right] + \frac{3}{2}\alpha_4 A\sum_{i=1}^{n}\phi_i''q_i\sum_{j=1}^{n}\phi_j'q_j\sum_{m=1}^{n}\phi_m'q_m + \frac{1}{2}\alpha_2 A\left[\frac{V_H'}{l}\sum_{i=1}^{n}\phi_i'q_i\sum_{j=1}^{n}\phi_j'q_j + 2\frac{V_H}{l}\sum_{i=1}^{n}\phi_i'q_i\sum_{j=1}^{n}\phi_j''q_j\right] - c_{\mathrm{s}}\sum_{i=1}^{n}\phi_i\dot{q}_i\right.$$

$$+ f_t\delta[s] - f_b\delta[s-l] - R_r\sum_{i=1}^{n}\phi_i\dot{q}_i\delta[s] - R_r\sum_{i=1}^{n}\phi_i\dot{q}_i\delta[s-l]\Bigg)\,\mathrm{d}s = 0. \tag{22}$$

Using the normalization conditions defined in Eqs. (21a) and (21b), and the nonlinear boundary conditions presented in Eqs. (14) and (15), the governing equation of kth temporal mode is simplified to

$$\begin{aligned}
&\ddot{q}_k + \omega_k^2 q_k + \sum_{i=1}^{n}\dot{q}_i\left[\int_0^l c_s\phi_k\phi_i\,\mathrm{d}s + R_r\phi_i\phi_k|_{s=0} + R_r\phi_i\phi_k|_{s=l}\right] + \int_0^l \phi_k' e_{33}A\frac{V_H}{l}\,\mathrm{d}s \\
&+ \sum_{i=1}^{n} q_i\int_0^l \alpha_3 A\phi_k'\phi_i'\frac{V_H}{l}\,\mathrm{d}s \\
&+ \frac{1}{2}\sum_{i=1}^{n}\sum_{j=1}^{n} q_iq_j\int_0^l \alpha_1 A\phi_k'\phi_i'\phi_j'\,\mathrm{d}s \\
&+ \frac{1}{2}\sum_{i=1}^{n}\sum_{j=1}^{n} q_iq_j\int_0^l \alpha_2 A\phi_i'\phi_j'\phi_k'\frac{V_H}{l}\,\mathrm{d}s \\
&+ \frac{1}{2}\sum_{i=1}^{n}\sum_{j=1}^{n}\sum_{m=1}^{n} q_iq_jq_m\int_0^l \alpha_4 A\phi_k'\phi_i'\phi_j'\phi_m'\,\mathrm{d}s \\
&= \phi_k(0)f_t - \phi_k(l)f_b.
\end{aligned} \tag{23}$$

Substituting the solution presented in Eq. (20b) in the circuit equation (13) and from Ohm's law, $\dot{\Psi} = -\frac{V}{R}$, we rewrite the sensing equation as

$$\begin{aligned}
&\sum_{i=1}^{n}\dot{q}_i e_{33}\frac{A}{l}\left[\phi_i(0) - \phi_i(l)\right] \\
&- \frac{1}{2}\alpha_3 A\frac{1}{l}\sum_{i=1}^{n}\sum_{j=1}^{n}\left(\dot{q}_iq_j + q_i\dot{q}_j\right)\int_0^l \phi_i'\phi_j'\,\mathrm{d}s \\
&- \frac{1}{6}\alpha_2 A\frac{1}{l}\sum_{i=1}^{n}\sum_{j=1}^{n}\sum_{m=1}^{n}\left(\dot{q}_iq_jq_m + \dot{q}_mq_jq_i + \dot{q}_mq_iq_m\right)\int_0^l \phi_i'\phi_j'\phi_m'\,\mathrm{d}s \\
&+ \epsilon_{33}^S A\frac{\dot{V}}{l} + \frac{V}{R} = 0.
\end{aligned} \tag{24}$$

In practice, the load resistance can be accompanied with a capacitor and/or an inductor to tune the power output [19]. However, in this work the analysis is restricted to a purely resistive load.

2.2 Approximate solution

To study the steady-state response characteristics of the coupled electromechanical Eqs. (23) and (24), we determine an approximate solution using the method of multiple scales [36,37]. Following Meesala and Hajj [50], we investigate the response characteristics near the first thickness resonant mode. Neglecting the contribution of higher thickness modes and assuming a proportional damping, we rewrite the governing equations of the first thickness mode as

$$\begin{aligned}
&\ddot{q} + \omega^2 q + 2\epsilon^2\mu\dot{q} + \epsilon\hat{\theta}V + \epsilon\delta_1 q^2 + \epsilon^2\delta_2 qV + \epsilon^2\delta_3 q^3 + \epsilon^3\delta_4 q^2 V \\
&= \frac{1}{2}\epsilon\Omega\left(F\mathrm{e}^{j\Omega t} + \overline{F}\mathrm{e}^{-j\Omega t}\right)
\end{aligned} \tag{25a}$$

$$-\hat{\theta}_V\dot{q} + C_p\dot{V} - \epsilon^2\delta_{4V}q^2\dot{q} - \epsilon\delta_{2V}q\dot{q} + \frac{V}{R} = 0, \tag{25b}$$

where

$$\epsilon^2\mu = \frac{1}{2}\left[2\zeta\omega + R_r\phi^2\Big|_{s=0} + R_r\phi^2\Big|_{s=l}\right],$$

$$\hat{\theta}_V = \epsilon\hat{\theta} = \left[\phi(l) - \phi(0)\right]\frac{e_{33}A}{l}, \tag{25c}$$

$$\begin{aligned}
\epsilon\delta_1 &= \frac{1}{2}A\alpha_1\int_0^l \phi'^3\,\mathrm{d}s, \quad \epsilon^2\delta_2 = \epsilon\delta_{2V} \\
&= \frac{A}{l}\alpha_3\int_0^l \phi'^2\,\mathrm{d}s, \epsilon^2\delta_3 = \frac{A\alpha_4}{2}\int_0^l \phi'^4\,\mathrm{d}s,
\end{aligned} \tag{25d}$$

$$\epsilon^3\delta_4 = \epsilon^2\delta_{4V} = \frac{A}{2l}\alpha_2\int_0^l \phi'^3\,\mathrm{d}s,$$

$$\epsilon F = \frac{j\rho_0 A Q}{4\pi d_t}\mathrm{e}^{-j\Omega\frac{d_t}{c_0}}\left[\phi(0) - \chi\phi(l)\mathrm{e}^{-j\Omega\tau}\right], \tag{25e}$$

and ϵ is a bookkeeping parameter that signifies the level to which the different terms in governing equations affect the response [36,37].

From the approximate solution and the amplitude response equation, Meesala and Hajj [50] showed that α_3 generates the response at 2Ω and that it does not affect the response at Ω. Moreover, they neglected the contribution of α_2 as it can be scaled to ϵ^3 as shown in Eq. (25a) and will potentially be masked by the electrical and mechanical noise. In reality, the acoustic wave generates higher harmonics as it propagates in the medium [26,27]. In this study, we neglect this transfer of energy to the higher harmonics which is

usually predominant at high source strengths. For the above-mentioned reasons, we drop the δ_2 and δ_4 terms in Eqs. (25a) and (25b) and solve the coupled system using the method of multiple scales.

We introduce three independent time scales T_0, T_1, and T_2 defined by

$$T_n = \epsilon^n t \qquad n = 0, 1, 2$$

and expand the derivatives up to $O(\epsilon^2)$ and write:

$$\frac{\mathrm{D}}{\mathrm{D}t} = \frac{\partial}{\partial T_0} + \epsilon\frac{\partial}{\partial T_1} + \epsilon^2\frac{\partial}{\partial T_2} \equiv D_0 + \epsilon D_1 + \epsilon^2 D_2 \tag{26a}$$

and

$$\frac{\mathrm{D}^2}{\mathrm{D}t^2} = \frac{\partial^2}{\partial T_0^2} + 2\epsilon\frac{\partial^2}{\partial T_1 \partial T_0} + \epsilon^2\left(2\frac{\partial^2}{\partial T_0 \partial T_2} + \frac{\partial^2}{\partial T_1^2}\right) \equiv D_0^2 + 2\epsilon D_0 D_1 + \epsilon^2\left(D_1^2 + 2D_0 D_2\right). \tag{26b}$$

The solutions of $q(t)$ and $V(t)$ are then expressed as

$$q(t,\epsilon) = q_0(T_0,T_1,T_2) + \epsilon q_1(T_0,T_1,T_2) + \epsilon^2 q_2(T_0,T_1,T_2) + \cdots \tag{27a}$$

$$V(t,\epsilon) = V_0(T_0,T_1,T_2) + \epsilon V_1(T_0,T_1,T_2) + \epsilon^2 V_2(T_0,T_1,T_2) + \cdots . \tag{27b}$$

To investigate the response near the first thickness mode, we let $\Omega = \omega + \epsilon\sigma$, where $\epsilon\sigma$ is a detuning parameter that represents the nearness of these frequencies. Substituting Eqs. (26a), (26b), (27a), and (27b) into Eqs. (25a), and (25b), retaining terms up to $O(\epsilon^2)$, we obtain

ϵ^0- order equations

$$D_0^2 q_0 + q_0\omega^2 = 0, \text{ and} \tag{28a}$$

$$RC_p D_0 V_0 - R\hat{\theta}_V D_0 q_0 + V_0 = 0. \tag{28b}$$

ϵ^1-order equations

$$D_0^2 q_1 + \omega^2 q_1 = -2\left(D_0 D_1 q_0\right) - \delta_1 q_0^2 - \hat{\theta} V_0 + \frac{j\rho_0 Q r_0^2 \Omega}{8d_t}\left[\phi(0) - \chi\phi(l)\mathrm{e}^{-j\Omega\tau}\right]\mathrm{e}^{j\Omega\left(T_0 - \frac{d_t}{c_0}\right)} - \frac{j\rho_0 Q r_0^2 \Omega}{8d_t}\left[\phi(0) - \chi\phi(l)\mathrm{e}^{j\Omega\tau}\right]\mathrm{e}^{-j\Omega\left(T_0 - \frac{d_t}{c_0}\right)}, \text{ and} \tag{29a}$$

$$RC_p D_0 V_1 - R\hat{\theta}_V D_0 q_1 + V_1 = -RC_p D_1 V_0 + R\hat{\theta}_V D_1 q_0. \tag{29b}$$

ϵ^2-order equations

$$D_0^2 q_2 + \omega^2 q_2 = -2D_0 D_1 q_1 - D_1^2 q_0 - 2D_0 D_2 q_0 - 2\mu_1 D_0 q_0 - \delta_3 q_0^3 - 2\delta_1 q_1 q_0 - \hat{\theta} V_1, \text{ and} \tag{30a}$$

$$RC_p D_0 V_2 - R\hat{\theta}_V D_0 q_2 + V_2 = -RC_p D_1 V_1 - RC_p D_2 V_0 + R\hat{\theta}_V D_1 q_1 + R\hat{\theta}_V D_2 q_0. \tag{30b}$$

From the ϵ^0-order equations, we obtain

$$q_0(T_0,T_1,T_2) = B(T_1,T_2)\mathrm{e}^{j\omega T_0} + c.c, \text{ and} \tag{31a}$$

$$V_0 = \frac{R\omega\hat{\theta}_V}{-j + R\omega C_p} B(T_1,T_2)\mathrm{e}^{j\omega T_0} + c.c. \tag{31b}$$

Substituting q_0 and V_0 in ϵ^1-order equation (29a) and eliminating the secular terms, we obtain

$$D_1 B = \frac{\rho_0 Q r_0^2 \Omega\left[\phi(0) - \chi\phi(l)\mathrm{e}^{-j\Omega\tau}\right]\mathrm{e}^{\left(-j\Omega\frac{d}{c_0} + j\sigma T_1\right)}}{16d\omega} + \frac{jBR\hat{\theta}\hat{\theta}_V}{2R\omega C_p - 2j}. \tag{32}$$

Removing the secular terms using the definition of $D_1 B$ in Eq. (32), we obtain

$$q_1(T_0,T_1,T_2) = \frac{\delta_1}{3\omega^2}B^2\mathrm{e}^{2jT_0\omega} - \frac{\delta_1}{\omega^2}B\bar{B} + c.c \tag{33a}$$

$$V_1(T_0,T_1,T_2) = \frac{R\hat{\theta}_V\left(R\omega C_p + j\right)^2}{48d_t\omega\left(R^2\omega^2 C_p^2 + 1\right)^2\left(R\omega C_p - j\right)}\Bigg[- 24jBd_t R\omega\hat{\theta}\hat{\theta}_V\mathrm{e}^{j\omega T_0} - \frac{3\rho_0 Q r_0^2\Omega\left(R\omega C_p - j\right)^2\mathrm{e}^{j\Omega\left(T_0 - \frac{d_t}{c_0} - \tau\right)}\left[\phi(0)\mathrm{e}^{j\Omega\tau} - \chi\phi(l)\right]}{R\Omega C_p - j} + \frac{32B^2 d_t\delta_1\mathrm{e}^{2j\omega T_0}\left(R\omega C_p - j\right)^3}{2R\omega C_p - j}\Bigg] + c.c. \tag{33b}$$

Using the solution equations for q_1 and V_1 in the ϵ^2-order equation (30a) and eliminating the secular terms, we obtain

$$D_2 B = \frac{1}{8}B\left(-8\mu_1 + \frac{R^2\hat{\theta}^2\hat{\theta}_V^2\left(1 - jR\omega C_p\right)}{\omega\left(R\omega C_p - j\right)^3}\right) + \frac{iB^2\bar{B}\left(9\delta_3\omega^2 - 10\delta_1^2\right)}{6\omega^3} - \Delta_1\rho_0 Q r_0^2\Omega\mathrm{e}^{j\epsilon\sigma T_0 - j\Omega\frac{d_t}{c_0}} \times\left[\phi(0) - \chi\phi(l)\mathrm{e}^{-j\Omega\tau}\right], \tag{34a}$$

where

$$\Delta_1 = \frac{R\hat{\theta}\hat{\theta}_V\left(R\Omega C_p + j\right) + 2\sigma\left(R\omega C_p - j\right)\left(R\Omega C_p - j\right)}{64d_t\omega^2\left(R\omega C_p - j\right)\left(R\Omega C_p - j\right)}. \tag{34b}$$

Using the chain rule of differentiation, we write

$$\dot{B} = \epsilon D_1 B + \epsilon^2 D_2 B. \tag{35}$$

Substituting the expressions for $D_1 B$ and $D_2 B$, respectively, from Eqs. (32) and (34a), we obtain the complex amplitude modulation equation. Now, we represent the complex amplitude as $B(T_1, T_2) = \frac{1}{2} a e^{j\beta(T_1,T_2)}$ and separate the real and imaginary parts to determine the amplitude and phase modulation equations, respectively, as

$$\begin{aligned}\dot{a} = {} & m_{(1,1)} a + m_{(1,2)} \sin\left(\gamma - \frac{d_t}{c_0}\Omega\right) \\ & + m_{(1,3)} \cos\left(\gamma - \frac{d_t}{c_0}\Omega\right) \\ & + m_{(1,4)} \sin\left(\gamma - \left[\frac{d_t}{c_0} + \tau\right]\Omega\right) \\ & + m_{(1,5)} \cos\left(\gamma - \left[\frac{d_t}{c_0} + \tau\right]\Omega\right), \text{ and} \end{aligned} \tag{36}$$

$$\begin{aligned}\dot{\gamma} = {} & \epsilon\sigma + m_{(2,1)} + m_{(2,2)} a^2 \\ & + \frac{1}{a}\left[m_{(2,3)} \sin\left(\gamma - \frac{d_t}{c_0}\Omega\right)\right. \\ & + m_{(2,4)} \cos\left(\gamma - \frac{d_t}{c_0}\Omega\right) \\ & + m_{(2,5)} \sin\left(\gamma - \left[\frac{d_t}{c_0} + \tau\right]\Omega\right) \\ & \left. + m_{(2,6)} \cos\left(\gamma - \left[\frac{d_t}{c_0} + \tau\right]\Omega\right)\right]. \end{aligned} \tag{37}$$

In deriving the amplitude and phase modulation equations, $\gamma = \epsilon\sigma t - \beta$ has been used to remove the explicit dependence on time in the equations. The coefficients $m_{(i,j)}$ are presented in "Appendix". By setting $\dot{a} = 0$ and $\dot{\gamma} = 0$, we find the steady-state amplitude a_0 and phase γ_0, for a given excitation condition, and write the approximate solution of Eqs. (25a) and (25b) as

$$u(s,t) = a_0 \phi(s) \cos(\Omega t - \gamma_0) + \cdots \tag{38a}$$

$$\begin{aligned} V(t) = {} & \frac{a_0 R \hat{\theta}_V \omega}{1 + R^2\omega^2 C_p^2}\left[R\omega C_p \cos(\Omega t\right. \\ & \left. - \gamma) - \sin(\Omega t - \gamma)\right] + \cdots. \end{aligned} \tag{38b}$$

3 Nonlinear parameter identification

Few investigations have considered nonlinear aspects of piezoelectric materials [28–33]. In this section, we present a parameter identification procedure [50] to determine α_1 and α_4 in the enthalpy density equation as defined above. To simplify the analysis, we consider a piezoelectric receiver that is freely suspended in air, where the radiation effects are negligible, and subject it to an electrical excitation. The parameter identification approach is based on using the approximate solution of the response of the receiver obtained with the method of multiple scales. This solution is then used to determine the nonlinear material parameters. To this end, we consider the actuation equation of the receiver and write it as

$$\ddot{q} + \omega^2 q + 2\epsilon^2\mu\dot{q} + \epsilon\delta_1 q^2 + \epsilon^2\delta_3 q^3 = -\epsilon\hat{\theta} V \tag{39}$$

where $V = \frac{1}{2}|V|\left(e^{j\Omega t} + e^{-j\Omega t}\right)$ and $\Omega = \omega + \epsilon\sigma$. Using the same timescales defined in Sect. 2.2, we express the solution of q as

$$\begin{aligned} q(t;\epsilon) = {} & q_0(T_0, T_1, T_2) + \epsilon q_1(T_0, T_1, T_2) \\ & + \epsilon^2 q_2(T_0, T_1, T_2) + \cdots \end{aligned} \tag{40}$$

Substituting the assumed solution and the timescales in Eq. (39), we obtain

ϵ^0*− order equation*

$$D_0^2 q_0 + q_0\omega^2 = 0 \tag{41}$$

ϵ^1*−order equation*

$$\begin{aligned} D_0^2 q_1 + \omega^2 q_1 = {} & -2(D_0 D_1 q_0) - \delta_1 q_0^2 \\ & - \frac{1}{2}\hat{\theta}|V|\left(e^{j\Omega t} + e^{-j\Omega t}\right) \end{aligned} \tag{42}$$

ϵ^2*−order equation*

$$\begin{aligned} D_0^2 q_2 + \omega^2 q_2 = {} & -2D_0 D_1 q_1 - D_1^2 q_0 \\ & - 2D_0 D_2 q_0 - 2\mu_1 D_0 q_0 \\ & - \delta_3 q_0^3 - 2\delta_1 q_1 q_0. \end{aligned} \tag{43}$$

Following a similar procedure to the one detailed in Sect. 2.2, we obtain

$$q_0(T_0, T_1, T_2) = B(T_1, T_2) e^{j\omega T_0} + c.c, \tag{44a}$$

$$D_1 B = -\frac{j|V|\hat{\theta}}{4\omega} e^{-j\sigma T_1} \tag{44b}$$

$$q_1(T_0, T_1, T_2) = -\frac{\delta_1}{\omega^2} B\bar{B} + \frac{\delta_1}{3\omega^2} B^2 e^{2j\omega T_0} + c.c, \tag{44c}$$

$$\begin{aligned} D_2 B = {} & -\mu_1 B - \frac{5j\delta_1^2}{3\omega^3} B^2\bar{B} + \frac{3j\delta_3}{2\omega} B^2\bar{B} \\ & - \frac{j\sigma\hat{\theta}}{8\omega^2}|V| e^{j\sigma T_1}. \end{aligned} \tag{44d}$$

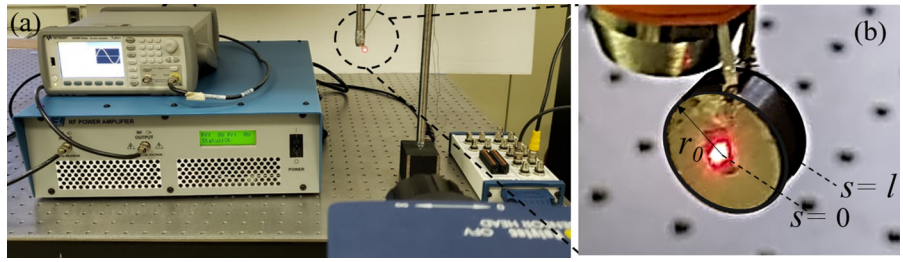

Fig. 3 **a** Dynamic actuation experimental apparatus including signal generator, power amplifier, and data acquisition system. **b** Piezoelectric disk with radius r_0 and thickness l in free–free boundary conditions, operating in thickness mode. The disk's surface velocity is measured by laser Doppler vibrometer

Representing the complex amplitude in polar form as $B = \frac{1}{2}ae^{j\beta}$ and defining $\gamma = \epsilon\sigma t - \beta$, we determine the amplitude and phase modulation equations as

$$\dot{a} = -\epsilon\frac{\hat{\theta}|V|}{2\omega}\sin\gamma + \epsilon^2\frac{\hat{\theta}\sigma|V|}{4\omega^2}\sin\gamma - \epsilon^2\mu_1 a \quad (45a)$$

$$\dot{\gamma} = \epsilon\left(\sigma - \frac{\hat{\theta}}{2a\omega}|V|\cos(\gamma)\right) + \epsilon^2\left(\frac{\sigma\hat{\theta}}{4a\omega^2}|V|\cos(\gamma) + \frac{5a^2\delta_1^2}{12\omega^3} - \frac{3a^2\delta_3}{8\omega}\right). \quad (45b)$$

Setting $\dot{a} = 0$ and $\dot{\gamma} = 0$, we obtain the steady-state amplitude response relation as

$$\sqrt{\frac{a_0^2\left(9a_0^2\delta_3\omega^2\epsilon - 10a^2\delta_1^2\epsilon - 24\sigma\omega^3\right)^2}{36\omega^2\hat{\theta}^2(\sigma\epsilon - 2\omega)^2} + \frac{16a_0^2\mu_1^2\omega^4\epsilon^2}{\hat{\theta}^2(\sigma\epsilon - 2\omega)^2}} = |V|. \quad (46)$$

The approximate solution is then written as

$$q(t) \approx a_0\cos(\gamma_0 - t\Omega) - \epsilon\delta_1\frac{a_0^2}{2\omega^2} + \epsilon\delta_1\frac{a_0^2}{6\omega^2}\cos(2\gamma_0 - 2t\Omega) + \cdots \quad (47)$$

or in the frequency domain as

$$q(\nu) \approx -\epsilon\delta_1\frac{a_0^2}{2\omega^2}\boldsymbol{\delta}(\nu) + a_0\boldsymbol{\delta}(\nu - \Omega) + \epsilon\delta_1\frac{a_0^2}{6\omega^2}\boldsymbol{\delta}(\nu - 2\Omega) + \cdots, \quad (48)$$

where a_0 and γ_0 are, respectively, the steady-state amplitude and phase and $\dot{\gamma} = 0$ and $\boldsymbol{\delta}$ is the Dirac delta function.

Using the amplitude response equation (46) and the approximate solution of Eq. (48), we note that the steady-state response at the forced frequency is a_0 and that is influenced by δ_1 and δ_3. Moreover, Eq. (48) shows that δ_1 is responsible for the generation of a dc component at $\nu = 0$ and the response at twice the forcing frequency. Using the value of δ_1, δ_3 can be determined from Eq. (46). From Eq. (25d), we note that the material nonlinear parameters, α_1 and α_4, are, respectively, related to δ_1 and δ_3. As such, one can identify δ_1 and δ_3 either by employing the steady-state amplitude response relation or from the amplitudes of the higher harmonics. The parameters α_1 and α_4 can then be evaluated using Eq. (25d).

4 Experiments

Experiments were conducted on an axially poled monolithic piezoelectric disk (modified PZT from PI GmbH) of length (thickness) $l = 4$ mm, radius $r_0 = 5$ mm, and mass per unit length of $m = 0.61$ g/m. The disk has silver electrodes covering the two outer faces and operates in the 33 (thickness) mode. The disk with free–free boundary conditions is shown in Fig. 3 for in-air actuation tests. During actuation experiments, the actuation voltage signal (harmonic X-cycle burst excitation) was generated by Keysight 33500B signal generator which is fed to E&I amplifier. The disk's surface velocity was measured by a laser Doppler vibrometer (LDV, Polytec OFV 5000/505) and acquired by NI DAQ system (BNC−2110). The data were collected at a sampling frequency of 10 MHz.

4.1 Parameter identification

4.1.1 Linear parameters

Surface velocity frequency response functions (FRFs) from in-air actuation experiments and model simula-

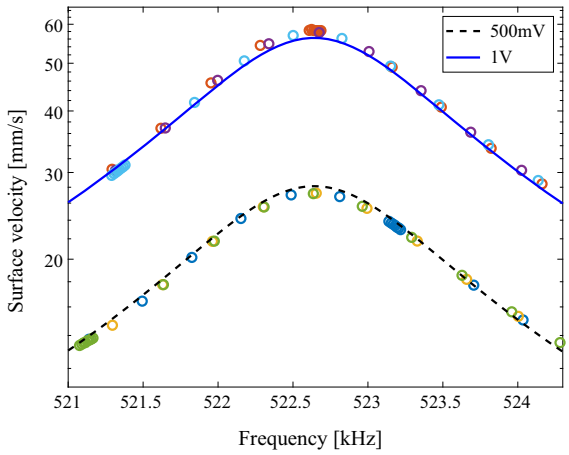

Fig. 4 Surface velocity versus excitation frequency; comparison between experimental data and model simulation using identified parameters at 500 mV and 1 V excitation amplitudes. The lines and circles, respectively, represent the model prediction and experimental data

tion are presented in Fig. 4. To identify the linear parameters, we consider 500 mV and 1 V excitation amplitudes and determine the velocity of the disk's surface in a frequency sweep in the neighborhood of the first thickness mode resonant frequency. We note that the strains generated for 500 mV and 1 V voltage amplitudes are not significant to trigger any material nonlinear behavior. As such, we drop the nonlinear terms in the actuation equation (39) and determine the amplitude of disk's surface velocity for a given voltage signal $V = |V| \cos(\Omega t)$, as

$$|\dot{u}|_{s=0} = \frac{\Omega\theta\phi(0)[\phi(0) - \phi(l)]}{\sqrt{\left(\omega^2 - \Omega^2\right)^2 + 4\zeta^2\omega^2\Omega^2}}|V|. \tag{49}$$

In determining Eq. (49), the acoustic radiation effects (resistive and reactive terms) are neglected as the ratio of acoustic impedance of air to that of PZT is very small ($\approx 10^{-5}$).

Using a least-square curve fit function, linear parameters are obtained as shown in Table 1. Figure 4 shows a good agreement between the experimental data and model prediction using the identified linear parameters for both 500 mV and 1 V excitation amplitudes.

Using the mode shape given by Eq. (20b) in conjunction with the orthogonality conditions presented in Eqs. (21a) and (21b), we obtain the mass normalized mode shape as

Table 1 Identified structural parameters of piezoelectric disk

Parameter [units]	Value
Natural frequency, $\omega/(2\pi)$ [kHz]	522.64
Young's modulus, $Y_{33} = m\omega^2 l^2/(A\pi^2)$ [GPa]	136.36
$\theta\phi(0)^2$ [cm^{-1} kg^{-1}]	3.04×10^2
Damping ratio (ζ)	1.65×10^{-3}

$$\phi(s) = 28.57 \cos\left(\frac{\pi}{l}s\right) \implies \phi(0) = -\phi(l) = 28.57 \text{ kg}^{-1/2}. \tag{50}$$

From the value of $\phi(0)$ in Eq. (50) and using the identified value of $\theta\phi(0)^2$, we determine the electromechanical coupling as $\theta = 3.73 \times 10^{-1}$ C/m.

4.1.2 Nonlinear parameters

A combined experimental–mathematical identification scheme that exploits the vibration response of the piezoelectric disk is implemented to estimate parameters representing nonlinear piezoelectric coefficients. We consider the piezoelectric disk with the geometric and material properties presented in Table 1. Then, following the parameter identification approach detailed in Sect. 3, and using the experimental setup for dynamic actuation shown in Fig. 3, the values of the nonlinear constitutive parameters are obtained.

Figure 5a, b shows, respectively, the time history of harmonic input actuation voltage measured across the transducer and the disk's surface velocity measured by LDV. The quality of the signals using 10 MHz sampling frequency is shown in the insets in Fig. 5a, b. Power spectra of these time series are, respectively, presented in Fig. 5c, d. It is worthy to note that, during the actuation tests, it was observed that the actuation input voltage that is measured across the disk varies in a frequency sweep for a constant voltage value set in the signal generator. This might be because of the inability of the control circuits of the amplifier/signal generator to respond to fast changes in the load impedance (impedance of receiver). Moreover, exerting high electric fields gradually increases the temperature of receiver [51] and affects the material properties and response characteristics like capacitance, electromechanical coupling, resonance frequency, and impedance [52–55]. In order to avoid the abovementioned implicit complicated behavior of the piezo-

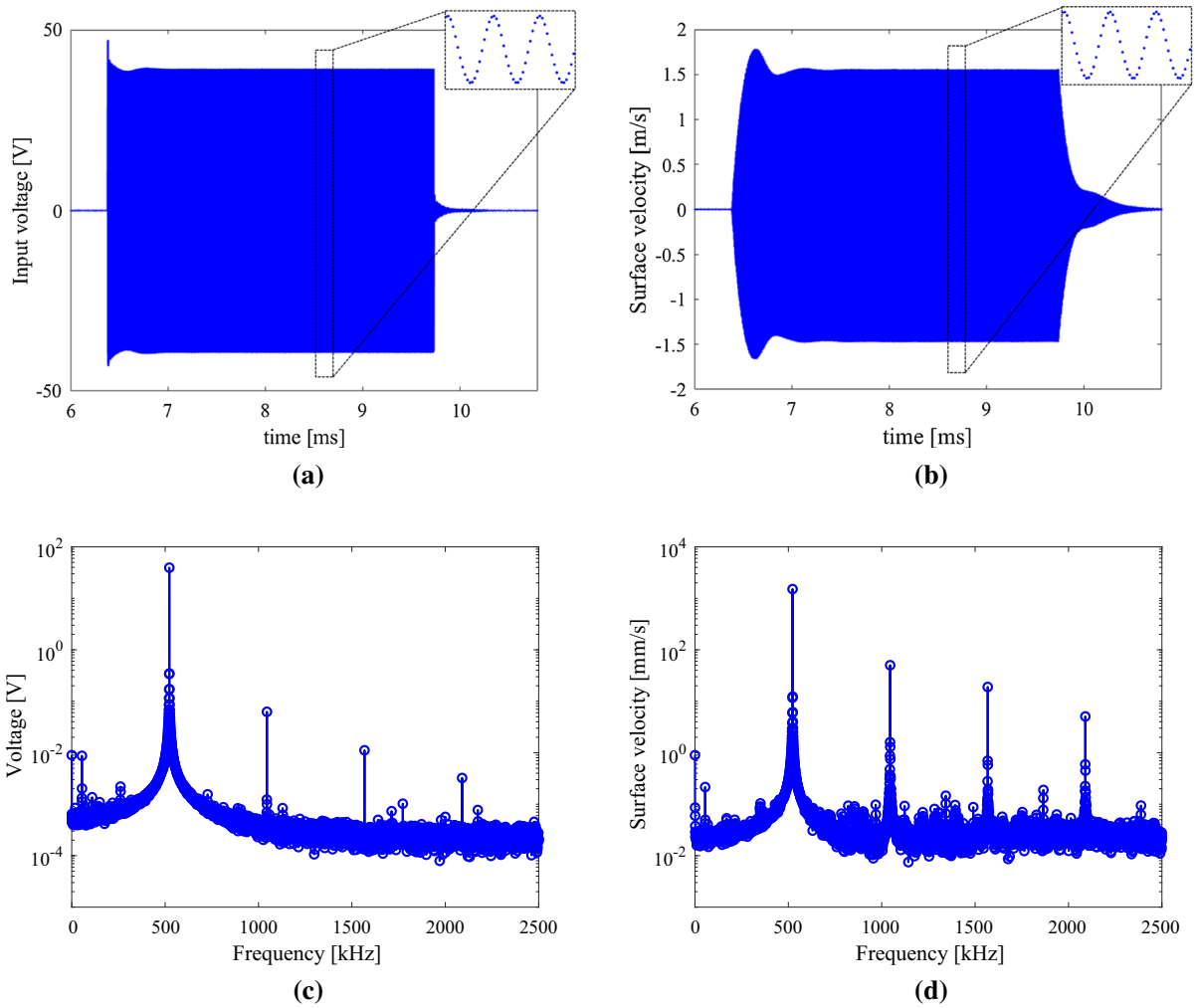

Fig. 5 Time series of the **a** input voltage to the piezoelectric disk in dynamic actuation and **b** disk's surface velocity measured by LDV for an excitation frequency of 522.5 kHz. Power spectrum of **c** the dynamic actuation and **d** disk's surface velocity

electric disk, we fixed the excitation frequency and performed a voltage sweep. For each excitation, the input voltage signal was fed for approximately 3.4 ms with a 10-min delay between consecutive excitation measurements. This is to ensure that the temperature of the receiver do not rise, which may alter the material properties, thereby creating the necessary conditions for identifying stable nonlinear material properties at room temperature.

Figure 5c shows the presence of higher harmonics in the input actuation voltage that are generated due to internal resonances in amplifier/signal generator and data acquisition system. For such an input excitation signal, the response at higher harmonics is due to the linear response at that particular frequency and due to nonlinear material properties. Subsequently, identifying the nonlinear material parameters from higher harmonics requires a laborious process of identifying the coefficients in governing equation of higher modes and understanding coupled circuit dynamics of signal generation and data acquisition. From Fig. 5d, we note that the higher harmonics' contribution to the response is negligible. Therefore, we use $\sqrt{2} \times$ RMS of the signal as the response amplitude at excitation frequency for the purpose of parameter identification. This estimate is favored over the spectral peaks to reduce the errors associated with the Fourier transform.

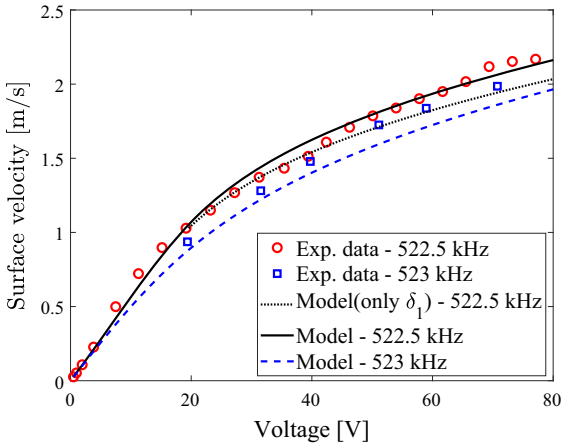

(a)

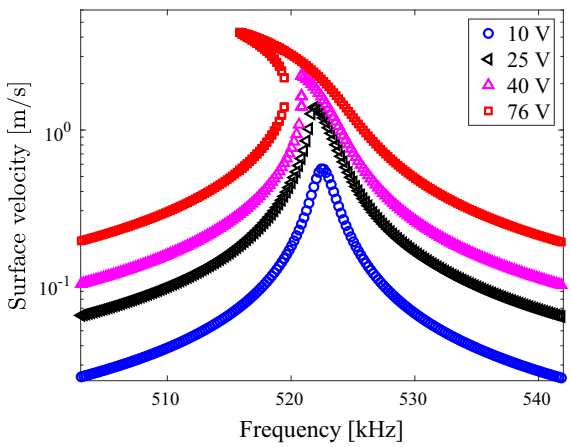

(b)

Fig. 6 Comparison between experimental data and model prediction (disk surface velocity vs. amplitude of input actuation voltage) for **a** nonlinear frequency response of the disk with identified parameters at 522.5 kHz and 523 kHz; Markers represent experimental data and lines represent the model prediction. **b** Frequency response predicted with the method of multiple scales using identified material parameters

Figure 6a shows the amplitude of surface velocity averaged over five experiments when increasing the voltage from 500 mV to 77 V at 522.5 kHz and 523 kHz. Figure 6a shows a linear response over the range between 500 mV and 15V and a saturation response beyond 15 V, which is a consequence of material nonlinearity. As a first step in identifying nonlinear parameters, we solve the amplitude response equation (46) only for δ_1 (i.e., we assume $\delta_3 = 0$) over the excitation range between 19 and 39 V and determine that $\delta_1 \approx 4.6 \times 10^{19}\ \mathrm{kg^{-1/2}\,m^{-1}s^{-2}}$. Yet, as shown in Fig. 6a, using just δ_1 underestimates the response over the excitation range 42–77 V. Therefore, it is necessary to identify the cubic nonlinear stiffness parameter, δ_3. Using the δ_1 determined previously, we solve the amplitude response equation (46) for δ_3 and obtain two solutions as $\delta_3^{soft} = 3.8 \times 10^{25}\ \mathrm{kg^{-1}\,m^{-2}s^{-2}}$ and $\delta_3^{hard} = 3.5 \times 10^{26}\ \mathrm{kg^{-1}\,m^{-2}s^{-2}}$, which, respectively, imply softening and hardening responses. To eliminate one of the solution, we note that the response measured at 523 kHz is smaller than the response at 522.5 kHz for a given excitation voltage as shown in Fig. 6a, suggesting that the nonlinearity is of softening type and chooses $\delta_3^{soft} = 3.8 \times 10^{25}\ \mathrm{kg^{-1}\,m^{-2}s^{-2}}$. Figure 6a also shows a good agreement between the experimental data and the response predicted by method of multiple scales with δ_1 and δ_3 identified using the data at 522.5 kHz. Since δ_1 and δ_3 are related to α_1 and α_4 by

$$\delta_1 = \frac{1}{2} A\alpha_1 \int_0^l \phi'^3\,\mathrm{d}s, \quad \text{and} \quad \delta_3 = \frac{A\alpha_4}{2} \int_0^l \phi'^4\,\mathrm{d}s, \tag{51}$$

we use the mode shape presented in Eq. (50) and determine the nonlinear constitutive relation parameters as $\alpha_1 = -61$ TPa and $\alpha_4 = 2.6$ PPa.

4.2 UAET in water

Having identified the linear and nonlinear material parameters in Sects. 4.1.1 and 4.1.2, we investigate the electromechanical response of the piezoelectric disk, when employed as a receiver subjected to a spherical acoustic wave excitation as shown in Fig. 1. The longitudinal strain axis of the receiver and the electrical poling axis (perpendicular to the surface electrodes) are coincident, and therefore the receiver disk is employed in the 33-mode piezoelectricity. The distance between the source and top surface of the receiver is set at $d_t = 40$ mm. For analysis, the capacitance, $C_p = 108.48$ pF, is used which is obtained from the data sheet provided by the manufacturer.

4.2.1 Modal acoustic–structure interaction and linear response

The piezoelectric material and wave propagation nonlinearities are negligible at low excitation source

strengths. Therefore, we drop the nonlinear terms in Eqs. (23) and (24) to determine the receiver's voltage output as

$$V(t) = \frac{j\Omega\hat{\theta}_V\left[\phi(0)f_\mathrm{t} - \phi(l)f_\mathrm{b}\right]\mathrm{e}^{j\Omega t}}{\left[-\Omega^2 + \omega^2 + j\Omega\left(2\zeta\omega + R_\mathrm{r}\left[\phi(0)^2 + \phi(l)^2\right]\right)\right]\left(C_p j\Omega + \frac{1}{R}\right) + j\Omega\hat{\theta}_V^2}, \tag{52}$$

where the mass normalized mode shape in water is determined as

$$\phi(s) = 28.5\left[\cos\left(738.8 \times s\right) - 3.1 \times 10^{-3}\sin\left(738.8 \times s\right)\right]. \tag{53}$$

Acoustic–structure interaction happens in UAET systems by two-way coupling of acoustic pressure waves in the fluid with the vibrations of the transmitter and receiver. The coupling mechanism of incident acoustic pressure on top and bottom surfaces of the receiver (in free–free boundary conditions as proposed by Shahab et al. [20]) for a given source strength with receiver's modal vibrations results in a net frequency-dependent modal force experienced by the receiver. It is pivotal to identify this frequency-dependent behavior as it affects the electromechanical response of the receiver. As such, we define the normalized modal force as

$$F_\mathrm{modal} = \frac{f_\mathrm{t}\mathrm{e}^{-j\Omega t}\phi(0) - f_\mathrm{b}\mathrm{e}^{-j\Omega t}\phi(l)}{\max\left(f_\mathrm{t}\mathrm{e}^{-j\Omega t}\phi(0) - f_\mathrm{b}\mathrm{e}^{-j\Omega t}\phi(l)\right)} = \frac{p_\mathrm{t}A\mathrm{e}^{-j\Omega t}\left[\phi(0) - \chi\mathrm{e}^{-j\Omega\tau}\phi(l)\right]}{\max\left(p_\mathrm{t}A\mathrm{e}^{-j\Omega t}\left[\phi(0) - \chi\mathrm{e}^{-j\Omega\tau}\phi(l)\right]\right)}, \tag{54}$$

where $p_\mathrm{t} = j\rho_0\Omega\frac{Q}{4\pi}\frac{1}{d_\mathrm{t}}\mathrm{e}^{j(\Omega t - \Omega d_\mathrm{t}/c_0)}$.

The phase difference of the vibration of top and bottom surfaces corresponding to the first thickness mode of the piezoelectric disk receiver is approximately π. In Eq. (54), the net modal force experienced by the receiver disk, which is placed in the far field of the spherical source (i.e., $l/d_\mathrm{t} << 1$), is minimum when $\mathrm{e}^{j\Omega\tau}$ is -1. This term can alternatively be represented as $k_0 l = (2n-1)\pi$, where $n = \lfloor\frac{\omega_0 l}{2\pi c_0} + \frac{1}{2}\rceil$ and $\lfloor\cdots\rceil$ represents the nearest integer function. This destructive interference happens due to acoustic–structure interaction wherein the acoustic pressure wave is coupled to the receiver and the modal response of the receiver is coupled back to the acoustic domain.

From the impedance analysis [20], the short- and open-circuit resonance frequencies of the receiver are identified as 521.6 kHz and 614.4 kHz, respectively. By choosing a frequency range between 470 and 660 kHz, which covers both short- and open-circuit natural frequencies, we present the net force experienced by the receiver (modal force defined in Eq. (54)) in Fig. 7a for different distances between the receiver and source. The excitation frequency is represented in terms of $k_0 l$ which ranges between 7.87 and 11 for the chosen frequency range. Figure 7a shows that a destructive interference occurs when $k_0 l = 3\pi$ or when $\Omega/(2\pi) = 562$ kHz, which is between the short- and open-circuit frequencies of the receiver. We note that the frequency at which destructive interference occurs, i.e., the net modal force is decreased, depends on the thickness of the receiver and the speed of sound in the fluid medium. In addition, the results in Fig. 7a show that the net force experienced by the receiver is subjected to greater destructive interference as the source-to-receiver distance is increased.

To investigate the optimal conditions of the receiver, the power output of the receiver (which is determined using Eq. (52)) due to a spherical source of source strength $Q = 10\,\mu\,\mathrm{m}^3/\mathrm{s}$, located at $d_\mathrm{t} = 40$ mm, is presented in Fig. 7b for a broad range of resistive electrical loads, R, and excitation frequencies. In agreement with typical piezoelectric energy harvesting systems, two peaks of power output are noted at the fundamental short- and open-circuit resonance frequencies. It is seen that the global peak happens at open-circuit condition. The corresponding optimal load (R_oc) is identified as 8.8 kΩ. From Fig. 7b, we note that the optimal loading at short-circuit condition (R_sc) is 586 Ω. Furthermore, the frequency corresponding to maximum power generated at R_sc is less than the short-circuit frequency. This contradicts the well-known fact that the coupled resonant frequency of a piezoelectric oscillator is greater than the short-circuit resonant frequency and that it increases with an increase in load resistance. This anomalous behavior is due to the decrease in the net force experienced by the receiver for a given source strength when increasing the excitation frequency near short-circuit conditions, as shown in Fig. 7a. On the other hand, the net force experienced by the receiver increases when increasing the excitation frequency near open-circuit conditions that conse-

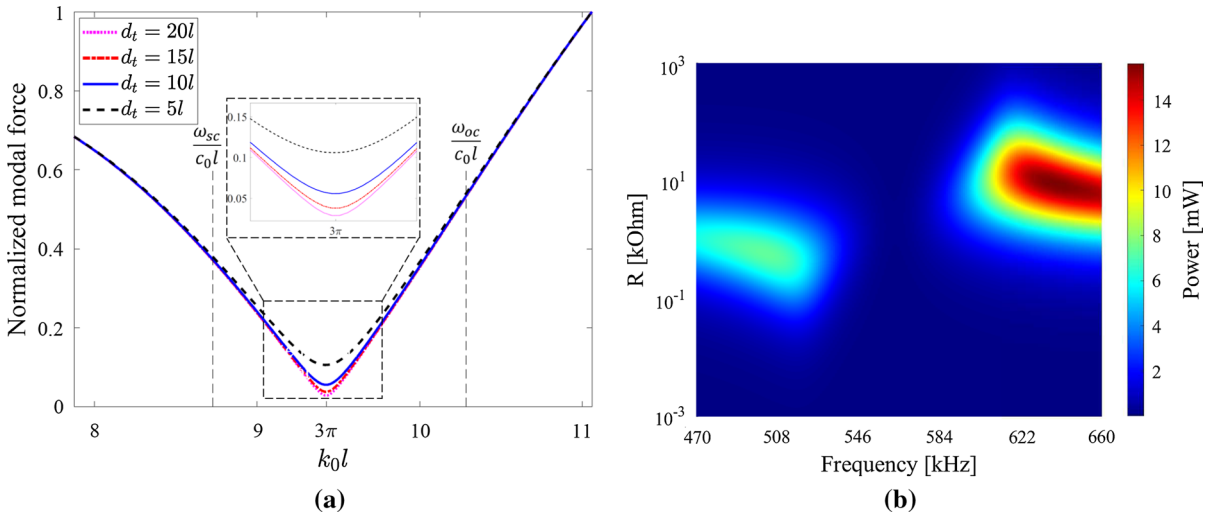

Fig. 7 **a** Modal force normalized by the maximum modal force as defined in Eq. (54), acting on the disk as a function of excitation frequency represented as $k_0 l$ for different source-to-receiver distances and **b** power output for the submerged piezoelectric receiver versus excitation frequency and load resistance using the analytical model for an acoustic source strength of $Q = 10\,\mu\text{m}^3/\text{s}$

quently increases the frequency corresponding to maximum power generated at 8.7 kΩ. It is relevant to point out the net damping in the system is a combination of structural and electrical damping and the resistive radiation impedance.

4.2.2 Nonlinear response

We investigate next the effect of the nonlinear parameters on the response and the receiver's electrical power output by employing the approximate solution determined using the method of multiple scales and given by Eqs. (38a) and (38b).

We note that the receiver's voltage output at optimal electrical loading for high source strengths is too high and hard to experimentally generate due to thermal inertia in the piezoelectric material that can vary material properties or degrade the disk. Heat generation within the piezoelectric actuator due to electrical and mechanical losses is a major concern for high-frequency applications. The properties such as capacitance, electromechanical coupling coefficient will evolve with temperature increasing the risk of unstable performance, especially near bifurcations. We chose a load resistance $R = 1\ \Omega$ which is closer to short-circuit conditions in our numerical simulations. We note that relatively low load resistances possess lower net electromechanical damping when compared to the optimum load resistances. Therefore, at short-circuit conditions, higher strains are induced at relatively low source strengths in comparison with the global optimum load resistance. Figure 8a shows, respectively, the top surface's displacement and the strain produced in the structure at the center of the disk (i.e., $s = l/2$), and Fig. 8b shows the power output as the source strength is increased from $Q = 10\,\mu\text{m}^3/\text{s}$ to $Q = 2\,\text{mm}^3/\text{s}$ over an excitation frequency range between 470 and 540 kHz. Figure 8a, b clearly demonstrates the manifestation of softening material nonlinearity when increasing the source strength. It can be concluded that the linear behavior that is represented by the solid lines is retained for source strengths up to 500 $\mu\text{m}^3/\text{s}$. We also note that the strain at $s = l/2$ induced in the receiver required to trigger the material nonlinearity is about 500–1000 $\mu\epsilon$. The good agreement of the power output determined from numerical simulations of the governing equations (25a) and (25b), with the predictions made by the method of multiple scales, is noted in Fig. 8b.

Based on the results of Fig. 8a, b, it can be concluded that for the receiver in consideration, the nonlinear behavior is triggered at a source strength of $Q = 2$ mm^3/s, for which the power generated at optimum load resistances will be impractical to reproduce in an exper-

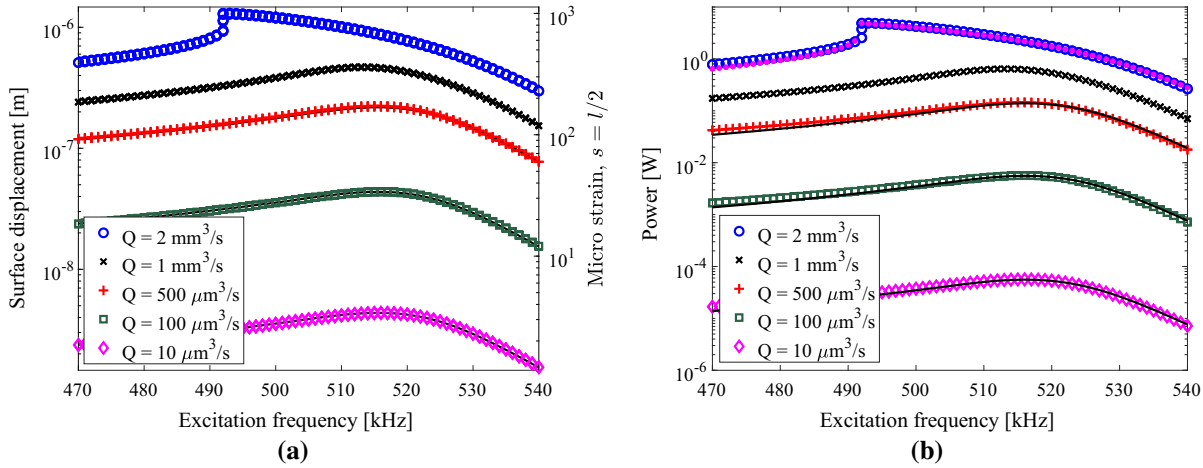

Fig. 8 **a** Displacement of the top surface along with strain induced in the piezoelectric disk at $s = l/2$, due to acoustic excitation and **b** power output predicted by the method of multiple scales for a load resistance of 1 Ω as the source strength is increased from $Q = 10\,\mu\text{m}^3/\text{s}$ to $Q = 2\,\text{mm}^3/\text{s}$. The dots represent data from numerical simulations and the solid line represents data from the analytical expression for linear response

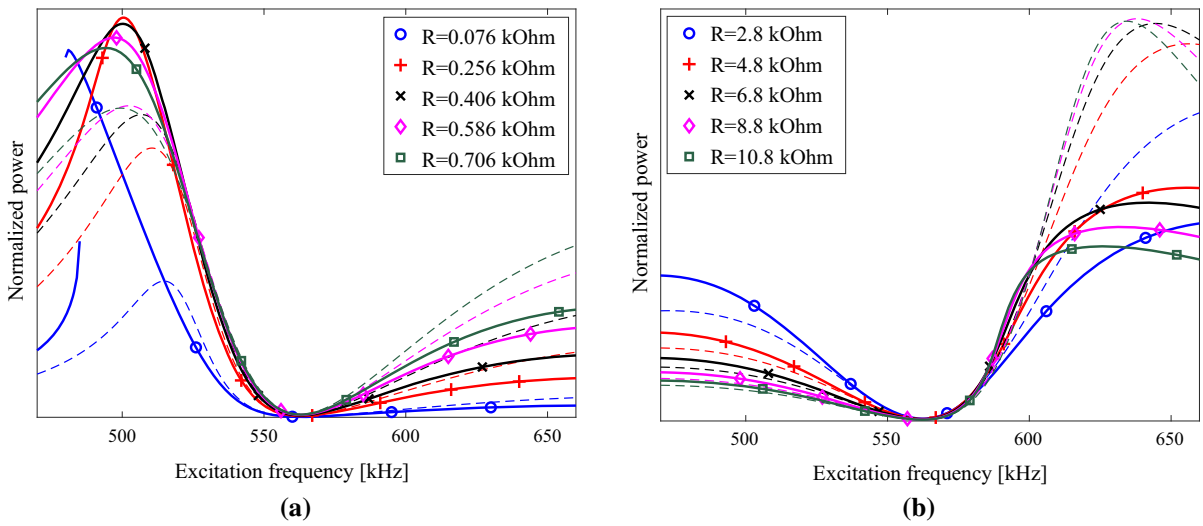

Fig. 9 Electrical power output as the excitation frequency is varied from 470 to 660 kHz **a** near the short-circuit optimum load resistance for a source strength of $Q = 2.5\ \mu\text{m}^3/\text{s}$ and **b** near the open-circuit optimum load resistance for a source strength of $Q = 7.5\ \mu\text{m}^3/\text{s}$. The dashed lines represent the linear response

imental setup. But for a different material whose nonlinear material parameters are much higher than the current receiver, the nonlinear behavior will be triggered at fairly lower source strengths, thereby generating experimentally achievable voltages. As such, it is important to understand the effects of a softening nonlinear behavior on the optimum load resistance. In particular, we investigated the effect of softening nonlinear behavior on the short- and open-circuit optimum load resistances as the excitation frequency is varied over the range between 470 and 660 kHz. Figure 9a shows the normalized power output for source strength, $Q = 2.5\ \text{mm}^3/\text{s}$ at different load resistances near the short-circuit optimum load resistance, $R_{\text{sc}} = 580\ \Omega$ ranging from 76 to 706 Ω with 30 Ω increments, and Fig. 9b shows the normalized power for $Q = 7.5$

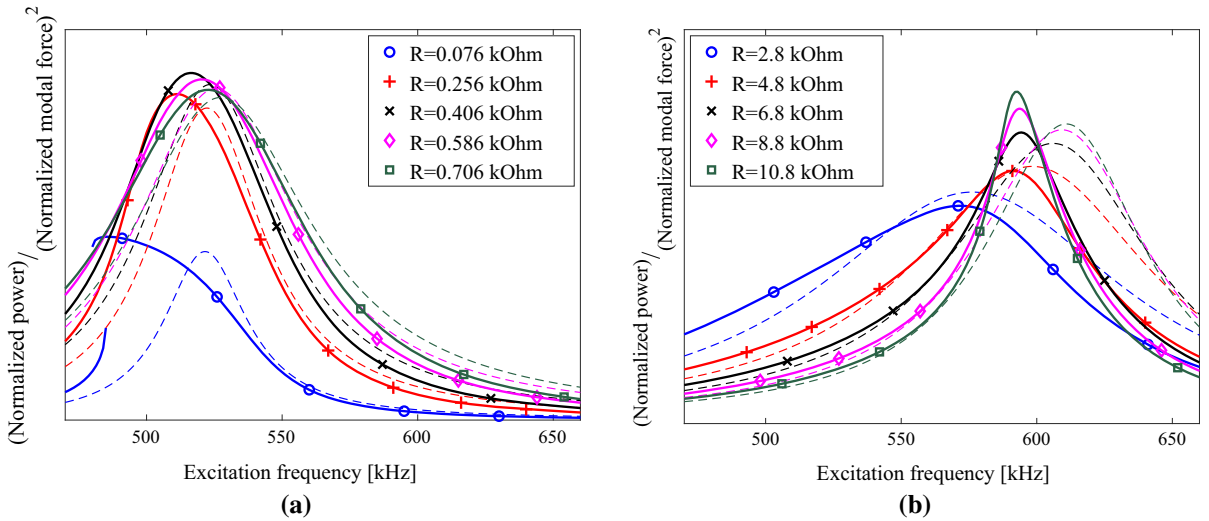

Fig. 10 Power output normalized with modal force as the excitation frequency is varied from 470 to 660 kHz **a** near the short-circuit optimum load resistance for a source strength of $Q = 2.5$ $\mu m^3/s$ and **b** near the open-circuit optimum load resistance for a source strength of $Q = 7.5$ $\mu m^3/s$. The dashed lines represent the linear response

mm^3/s near the open-circuit optimum load resistance ranging from 2.8 to 10.8 kΩ with 0.4 kΩ increments. The reason for choosing a higher source strength for the open-circuit configuration is because the net electromechanical damping is highest near the open-circuit optimum load resistance (or global optimum load resistance). Figure 9a shows an increase in the power output as the load resistance is decreased from 706 to 256 Ω, but the power output decreases when the load resistance is varied from 256 to 76 Ω, showing a shift in the local optimum resistance from 580 to 256 Ω. By comparing with the linear response for that load resistance, denoted by dashed lines, we note a shift in peaks as a consequence of the softening nonlinear behavior. Figure 9a also shows a dominant nonlinear behavior for a load resistance of $R = 76$ Ω, but it is interesting to note that 76 Ω is not the local optimum load resistance. Figure 9b shows a similar trend with a shift in the optimum load resistance from 8.8 to 4.8 kΩ.

In order to clearly visualize the nonlinear behavior, we normalize the power output with the modal force experienced by the receiver and present the modal force normalized power trend for short- and open-circuit optimum load configurations, respectively, in Fig. 10a, b. Figure 10a shows a prominent shift in the peak at lower load resistances, suggesting a higher nonlinear response at lower load resistances in the considered range of short-circuit load resistances. This is because the decrease in load resistance decreases the coupled resonant frequency and, by following the modal forcing trend presented in Fig. 7a, it experiences a higher modal force for a given source strength, thereby generating higher strains and higher nonlinear response. From Fig. 9a, recalling that the local optimum load resistance is decreased from 560 to 200 Ω, we conclude that the softening nonlinearity in conjunction with the current modal forcing trend near short-circuit range results in a decrease in the local optimum load resistance. By inspecting the modal force normalized power output in Fig. 10b, we note more pronounced shifts in the peak at higher load resistances 8.8 kΩ and 10.8 kΩ compared to the lower ones, which is not visually obvious in Fig. 9b. From Fig. 7a, the modal force increases when increasing the frequency over a range close to the open-circuit frequency. One would imagine that because the modal forcing trend near the open-circuit frequency is opposite to the trend near the short-circuit frequency, the optimum load resistance should increase. On the contrary, from Fig. 9b, we recall that the optimum load resistance decreased from 8.8 to 4.8 kΩ. This is because, although a receiver with higher open-circuit range load resistances experiences a larger force, the softening nonlinearity shifts the peak to a frequency corresponding to a lower modal force, thereby generating lower power. Therefore, the softening nonlinear behavior, in this case, is not aiding the

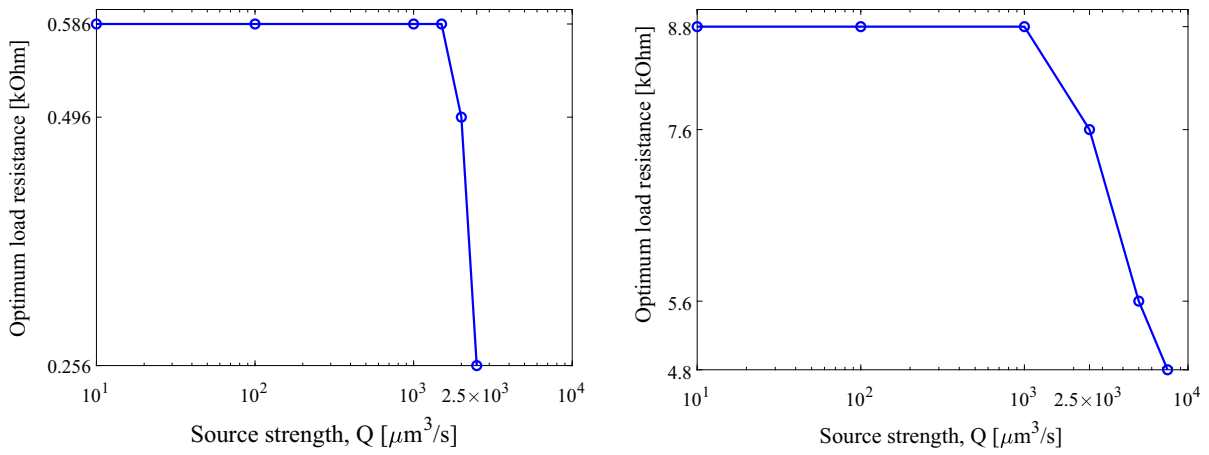

Fig. 11 Optimal load resistance versus source strength **a** near short-circuit and **b** near open-circuit optimum load resistances

response and thereby resistances leading to lower nonlinear behavior produce higher powers.

Figure 11a, b summarizes the change in optimum load resistance, respectively, over the short-circuit optimum load resistance range between 76 and 706 Ω with 30 Ω increments as the source strength is increased from $Q = 10$ μm^3/s to $Q = 2.5$ mm^3/s and in open-circuit optimum load resistance range (2.8–10.8 kΩ with 0.4 kΩ increments) as the source strength is decreased from $Q = 10$ μm^3/s to $Q = 7.5$ mm^3/s. Figure 11a, b shows a constant optimum load resistance, respectively, up to $Q = 1.5$ mm^3/s and $Q = 1$ mm^3/s and a gradual decrease in optimum load resistance at higher strengths as a consequence of softening material nonlinear response and modal forcing trend. From Fig. 11a, b, it is inferred that the curve is much steeper near the short-circuit optimum load resistance in comparison with the open one because the modal forcing trend causes the nonlinearity to be more pronounced and shifts the optimum load resistance near short-circuit optimum load resistance unlike near the open-circuit conditions.

5 Conclusions

We presented a mathematical framework to analyze the material nonlinear behavior in UAET systems. The governing and electrical circuit equations of a piezoelectric receiver disk, with free–free boundary conditions, subjected to a spherical acoustic excitation in a fluid medium were derived using generalized Hamilton's principle, followed by a Galerkin's weighted residual method. The nonlinear governing equations were then solved using the method of multiple scales to determine the approximate solution. To characterize the material nonlinearity, we implemented a parameter identification scheme based on the approximate solution of the actuation equation subjected to an electrical excitation. The parameter identification scheme was validated experimentally by identifying nonlinear stiffness parameters that captured the softening-type nonlinearity observed. From the analytical model, we demonstrated that the net modal force experienced by the receiver as a result of phase difference of acoustic waves on receiver's surfaces and its relative modal interaction follows a nontrivial trend by exhibiting a destructive behavior with respect to the excitation frequency, for a given source strength, and that it affects the receiver's response. We determined that, for a given receiver's dimensions, the excitation frequency at which destructive behavior occurs depends on the velocity of sound in the medium. By considering different source-to-receiver distances, d_t, we demonstrated that the destructive interference is stronger at larger d_t values. By using the approximate solution to the nonlinear governing and electrical circuit equation in conjunction with the identified material parameters, we demonstrated the softening behavior in the receiver's power output by choosing water as a fluid medium. We noted that at high source strengths, the short- and open-circuit optimum load resistances determined from the

linear analysis will no longer produce the highest power for a given source strength and that optimum load resistance shifts toward lower values. We concluded that this response is a consequence of the modal force trend and the softening-type material nonlinearity of the receiver. Finally, we determined that the shift is a function of source strength.

Acknowledgements This work was supported by the National Science Foundation Grant No. ECCS−1711139, which is gratefully acknowledged.

Compliance with ethical standards

Conflict of interest The authors declare that they have no conflict of interest.

6 Appendix

$$m_{(1,1)} = -\epsilon^2\mu_1 + \frac{R\epsilon\hat{\theta}\hat{\theta}_V\left(R^2\epsilon\hat{\theta}C_p\hat{\theta}_V\left(R^2\omega^2C_p^2-1\right)-\left(R^2\omega^2C_p^2+1\right)^2\right)}{4\left(R^2\omega^2C_p^2+1\right)^3} \tag{55}$$

$$m_{(1,2)} = \frac{\rho_0 Q r_0^2 R\Omega\epsilon^2\phi(0)\hat{\theta}\hat{\theta}_V\left(R^2\Omega C_p^2(2\omega+\Omega)-1\right)}{32d_t\omega^2\left(R^2\omega^2C_p^2+1\right)\left(R^2\Omega^2C_p^2+1\right)} \tag{56}$$

$$m_{(1,3)} = \frac{\rho_0 Q r_0^2\Omega\epsilon\phi(0)}{32d_t\omega^2}\left[\frac{R^2\epsilon\hat{\theta}C_p\hat{\theta}_V\left(-R^2\omega\Omega^2C_p^2+\omega+2\Omega\right)}{\left(R^2\omega^2C_p^2+1\right)\left(R^2\Omega^2C_p^2+1\right)}+4\omega-2\sigma\epsilon\right] \tag{57}$$

$$m_{(1,4)} = -\chi\frac{\phi(l)}{\phi(0)}m_{(1,2)},\quad m_{(1,5)} = -\chi\frac{\phi(l)}{\phi(0)}m_{(1,3)} \tag{58}$$

$$m_{(2,1)} = \frac{R^2\epsilon\hat{\theta}\hat{\theta}_V}{8\omega\left(R^2\omega^2C_p^2+1\right)^3}\left[\epsilon\hat{\theta}\hat{\theta}_V\left(R^4\omega^4C_p^4 - 6R^2\omega^2C_p^2+1\right) = -4C_p\left(R^2\omega^3C_p^2+\omega\right)^2\right] \tag{59}$$

$$m_{(2,2)} = \frac{\epsilon^2\left(10\delta_1^2-9\delta_3\omega^2\right)}{24\omega^3} \tag{60}$$

$$m_{(2,3)} = \frac{\rho_0 Q r^2\epsilon\phi_0\Omega}{32d_t\omega^2\left(R^2\omega^2C_p^2+1\right)\left(R^2C_p^2\Omega^2+1\right)}\left[R^2\epsilon\hat{\theta}C_p\hat{\theta}_V\left(R^2\omega C_p^2\Omega^2\ -3\omega-2\sigma\epsilon\right)+2(\sigma\epsilon-2\omega)\left(R^2\omega^2C_p^2+1\right)\left(R^2C_p^2\Omega^2+1\right)\right] \tag{61}$$

$$m_{(2,4)} = \frac{\rho_0 Q r^2 R\epsilon^2\phi_0\hat{\theta}\hat{\theta}_V\Omega}{32d_t\omega^2\left(R^2\omega^2C_p^2+1\right)\left(R^2C_p^2\Omega^2+1\right)}\left[R^2C_p^2\Omega(2\omega+\Omega)-1\right] \tag{62}$$

$$m_{(2,5)} = -\chi\frac{\phi(l)}{\phi(0)}m_{(2,3)},\ \text{and}\ \ m_{(2,6)} = -\chi\frac{\phi(l)}{\phi(0)}m_{(2,4)} \tag{63}$$

References

1. Kazmierkowski, M.P., Moradewicz, A.J.: Unplugged but connected: review of contactless energy transfer systems. IEEE Ind. Electron. Mag. **6**(4), 47–55 (2012)
2. Shidujaman, M., Samani, H., Arif, M.: Wireless power transmission trends. In: 2014 International Conference on Informatics, Electronics & Vision (ICIEV), pp. 1–6. IEEE (2014)
3. Kurs, A., Karalis, A., Moffatt, R., Joannopoulos, J .D., Fisher, P., Soljačić, M.: Wireless power transfer via strongly coupled magnetic resonances. Science **5834**(317), 83–86 (2007)
4. Dai, J., Ludois, D.C., et al.: A survey of wireless power transfer and a critical comparison of inductive and capacitive coupling for small gap applications. IEEE Trans. Power Electron. **30**(11), 6017–6029 (2015)
5. Brown, W.C.: The history of power transmission by radio waves. IEEE Trans. Microw. Theory Tech. **32**(9), 1230–1242 (1984)
6. Roes, M.G., Duarte, J.L., Hendrix, M.A., Lomonova, E.A.: Acoustic energy transfer: a review. IEEE Trans. Ind. Electron. **60**(1), 242–248 (2013)
7. Kawanabe, H., Katane, T., Saotome, H., Saito, O., Kobayashi, K.: Power and information transmission to implanted medical device using ultrasonic. Jpn. J. Appl. Phys. **40**(5S), 3865 (2001)
8. Suzuki, S.-N., Kimura, S., Katane, T., Saotome, H., Saito, O., Kobayashi, K.: Power and interactive information transmission to implanted medical device using ultrasonic. Jpn. J. Appl. Phys. **41**(5S), 3600 (2002)
9. Maleki, T., Cao, N., Song, S.H., Kao, C., Ko, S.-C., Ziaie, B.: An ultrasonically powered implantable micro-oxygen generator (imog). IEEE Trans. Biomed. Eng. **58**(11), 3104–3111 (2011)
10. Ozeri, S., Shmilovitz, D.: Simultaneous backward data transmission and power harvesting in an ultrasonic transcutaneous energy transfer link employing acoustically dependent electric impedance modulation. Ultrasonics **54**(7), 1929–1937 (2014)
11. Basaeri, H., Christensen, D.B., Roundy, S.: A review of acoustic power transfer for bio-medical implants. Smart Mater. Struct. **25**(12), 123001 (2016)
12. Christensen, D.B., Roundy, S.: Ultrasonically powered piezoelectric generators for bio-implantable sensors: plate versus diaphragm. J. Intell. Mater. Syst. Struct., **27**(8), 1092–1105 (2016)
13. Bakhtiari-Nejad, M., Elnahhas, A., Hajj, M.R., Shahab, S.: Acoustic holograms in contactless ultrasonic power transfer systems: modeling and experiment. J. Appl. Phys. **124**(24), 244901 (2018)
14. Hu, Y., Zhang, X., Yang, J., Jiang, Q.: Transmitting electric energy through a metal wall by acoustic waves using piezoelectric transducers. IEEE Trans. Ultrason. Ferroelectr. Freq. Control **50**(7), 773–781 (2003)
15. Sherrit, S., Badescu, M., Bao, X., Bar-Cohen, Y., Chang, Z.: Efficient electromechanical network model for wireless acoustic-electric feed-throughs. In: Smart Structures and Materials 2005: Smart Sensor Technology and Measurement Systems, vol. 5758, pp. 362–373. International Society for Optics and Photonics (2005)

16. Bao, X., Biederman, W., Sherrit, S., Badescu, M., Bar-Cohen, Y., Jones, C., Aldrich, J., Chang, Z.: High-power piezoelectric acoustic-electric power feedthru for metal walls. In: Industrial and Commercial Applications of Smart Structures Technologies 2008, vol. 6930, p. 69300Z. International Society for Optics and Photonics (2008)
17. Zaid, T., Saat, S., Yusop, Y., Jamal, N.: Contactless energy transfer using acoustic approach-a review. In: 2014 International Conference on Computer, Communications, and Control Technology (I4CT) , pp. 376–381. IEEE (2014)
18. Awal, M.R., Jusoh, M., Sabapathy, T., Kamarudin, M.R., Rahim, R.A.: State-of-the-art developments of acoustic energy transfer. Int. J. Antennas Propag. **2016** (2016)
19. Shahab, S., Erturk, A.: Contactless ultrasonic energy transfer for wireless systems: acoustic-piezoelectric structure interaction modeling and performance enhancement. Smart Mater. Struct. **23**(12), 125032 (2014)
20. Shahab, S., Gray, M., Erturk, A.: Ultrasonic power transfer from a spherical acoustic wave source to a free-free piezoelectric receiver: modeling and experiment. J. Appl. Phys. **117**(10), 104903 (2015)
21. Gorostiaga, M., Wapler, M., Wallrabe, U.: Analytic model for ultrasound energy receivers and their optimal electric loads. Smart Materials and Structures **26**(8), 085003 (2017)
22. Gorostiaga, M., Wapler, M., Wallrabe, U.: Analytic model for ultrasound energy receivers and their optimal electric loads ii: Experimental validation. Smart Mater. Struct. **26**(10), 105021 (2017)
23. Tseng, V.F.G., Bedair, S.S., Lazarus, N.: Acoustic wireless power transfer with receiver array for enhanced performance. In: 2017 IEEE Wireless Power Transfer Conference (WPTC), pp. 1–4 . IEEE (2017)
24. Tseng, V.F.-G., Bedair, S.S., Lazarus, N.: Phased array focusing for acoustic wireless power transfer. IEEE Trans. Ultrason. Ferroelectr. Freq. Control **65**(1), 39–49 (2018)
25. Christensen, D.B., Roundy, S.: Non-dimensional analysis of depth, orientation, and alignment in acoustic power transfer systems. Smart Mater. Struct. **27**, 125013 (2018)
26. Hamilton, M .F., Blackstock, D .T., et al.: Nonlinear Acoustics, vol. 1. Academic press, San Diego (1998)
27. Rozanova-Pierrat, A.: Mathematical analysis of khokhlov-zabolotskaya-kuznetsov (kzk) equation. Prepint of Laboratory Jaques-Louis Lions, Paris **6**, 1–69 (2006)
28. Aurelle, N., Guyomar, D., Richard, C., Gonnard, P., Eyraud, L.: Nonlinear behavior of an ultrasonic transducer. Ultrasonics **34**(2–5), 187–191 (1996)
29. Guyomar, D., Aurelle, N., Eyraud, L.: Piezoelectric ceramics nonlinear behavior. application to langevin transducer. J. de Phys. III 7 **6**, 1197–1208 (1997)
30. Von Wagner, U., Hagedorn, P.: Piezo-beam systems subjected to weak electric field: experiments and modelling of non-linearities. J. Sound Vib. **256**(5), 861–872 (2002)
31. Mahmoodi, S.N., Jalili, N., Daqaq, M.F.: Modeling, nonlinear dynamics, and identification of a piezoelectrically actuated microcantilever sensor. IEEE/ASME Trans. Mechatron. **13**(1), 58–65 (2008)
32. Stanton, S.C., Erturk, A., Mann, B.P., Inman, D.J.: Nonlinear piezoelectricity in electroelastic energy harvesters: modeling and experimental identification. J. Appl. Phys. **108**(7), 074903 (2010)
33. Leadenham, S., Erturk, A.: Unified nonlinear electroelastic dynamics of a bimorph piezoelectric cantilever for energy harvesting, sensing, and actuation. Nonlinear Dyn. **79**(3), 1727–1743 (2015)
34. Meesala, V.C., Hajj, M.R., Shahab, S.: Modeling electroelastic nonlinearities in ultrasound acoustic energy transfer systems. In: Active and Passive Smart Structures and Integrated Systems XII, vol. 10595, p. 105951G . International Society for Optics and Photonics(2018)
35. Kinsler, L.E., Frey, A.R., Coppens, A.B., Sanders, J.V. (eds.): Fundamentals of acoustics, 4th edn, p. 560. Wiley, Hoboken (1999). ISBN 0-471-84789-5
36. Nayfeh, A.H., Mook, D.T.: Nonlinear Oscillations. Wiley, Hoboken (2008)
37. Nayfeh, A.H.: Introduction to perturbation techniques. Wiley, Hoboken (2011)
38. Crandall, S.H.: Dynamics of mechanical and electromechanical systems. McGraw-Hill, New York (1968)
39. Hagood, N.W., Chung, W.H., Von Flotow, A.: Modelling of piezoelectric actuator dynamics for active structural control. J. Intell. Mater. Syst. Struct. **1**(3), 327–354 (1990)
40. Sodano, H.A.: Macro-fiber composites for sensing, actuation and power generation. Ph.D. thesis, Virginia Tech (2003)
41. Anton, S.R.: Multifunctional piezoelectric energy harvesting concepts. Ph.D. thesis, Virginia Tech (2011)
42. Shaw, E.: On the resonant vibrations of thick barium titanate disks. J. Acoust. Soc. Am. **28**(1), 38–50 (1956)
43. Ikegami, S., Ueda, I., Kobayashi, S.: Frequency spectra of resonant vibration in disk plates of $PbTiO_3$ piezoelectric ceramics. J. Acoust. Soc. Am. **55**(2), 339–344 (1974)
44. Ueha, S., Sakuma, S., Mori, E.: Measurement of vibration velocity distributions and mode analysis in thick disks of $Pb(Zr{\cdot}Ti)O_3$. J. Acoust. Soc. Am. **73**(5), 1842–1847 (1983)
45. Guo, N.: The vibration characteristics of piezoelectric discs. Ph.D. thesis, University of London (1989)
46. Kunkel, H., Locke, S., Pikeroen, B.: Finite-element analysis of vibrational modes in piezoelectric ceramic disks. IEEE Trans. Ultrason. Ferroelectr. Freq. Control **37**(4), 316–328 (1990)
47. Guo, N., Cawley, P., Hitchings, D.: The finite element analysis of the vibration characteristics of piezoelectric discs. J. Sound Vib. **159**(1), 115–138 (1992)
48. Butler, J.L., Sherman, C.H.: Transducers and Arrays for Underwater Sound. Springer, Berlin (2016)
49. Meirovitch, L.: Fundamentals of Vibrations. Waveland Press, Long Grove (2010)
50. Meesala, V.C., Hajj, M.R.: Identification of nonlinear piezoelectric coefficients. J. Appl. Phys. **124**(6), 065112 (2018)
51. Gonnard, P., Perrin, V., Briot, R., Guyomar, D., Albareda, A.: Characterization of the piezoelectric ceramic mechanical nonlinear behavior. In: Proceedings of the Eleventh IEEE International Symposium on Applications of Ferroelectrics, 1998 (ISAF 98), pp. 353–356. IEEE (1998)
52. Jaffe, H., Berlincourt, D.: Piezoelectric transducer materials. Proc. IEEE **53**(10), 1372–1386 (1965)
53. Wang, D., Fotinich, Y., Carman, G.P.: Influence of temperature on the electromechanical and fatigue behavior of piezoelectric ceramics. J. Appl. Phys. **83**(10), 5342–5350 (1998)

54. Wolf, R., Trolier-McKinstry, S.: Temperature dependence of the piezoelectric response in lead zirconate titanate films. J. Appl. Phys. **95**(3), 1397–1406 (2004)
55. Chen, Y., Liang, D., Wang, Q., Zhu, J.: Microstructures, dielectric, and piezoelectric properties of w/cr co-doped bi4ti3o12 ceramics. J. Appl. Phys. **116**(7), 074108 (2014)

Publisher's Note Springer Nature remains neutral with regard to jurisdictional claims in published maps and institutional affiliations.